Mechanically robust transparent anti-icing coatings : roles of dispersion status of titanate nanotubes

Wu, Xinghua; Tang, Yuxin; Silberschmidt, Vadim V.; Wilson, Peter; Chen, Zhong

2018

Wu, X., Tang, Y., Silberschmidt, V. V., Wilson, P., & Chen, Z. (2018). Mechanically robust transparent anti-icing coatings : roles of dispersion status of titanate nanotubes. Advanced Materials Interfaces, 5(18), 1800773-. doi:10.1002/admi.201800773

https://hdl.handle.net/10356/107520

https://doi.org/10.1002/admi.201800773

WILEY-VCH

DOI: 10.1002/ ((please add manuscript number))
Article type: ((**Full Paper**))

Mechanically Robust Transparent Anti-icing Coatings: Roles of Dispersion Status of Titanate Nanotubes

*Xinghua Wu[1], Yuxin Tang[1], Vadim V. Silberschmidt[2], Peter Wilson[3], Zhong Chen**

X.H. Wu 1, PhD student. Y.X. Tang 1, Dr. Tang. V. V. Silberschmidt 2, Prof. Silberschmidt.
P. Wilson 3, Prof. Wilson, Z. Chen 1, Prof. Chen.
X.H. Wu, Dr. Tang, Prof. Chen.
School of Materials Science and Engineering, Nanyang Technological University, 50 Nanyang Avenue, 639798, Singapore
E-mail: aszchen@ntu.edu.sg
Prof. Silberschmidt, Author 2
Wolfson School of Mechanical, Electrical and Manufacturing Engineering, Loughborough University, Loughborough, Leicestershire LE11 3TU, UK
Prof. Wilson Author 3
Institute for Marine and Antarctic Science, University of Tasmania, Hobart 7000, Australia and Honors College, University of South Florida, Tampa 33620, USA

Keywords: anti-icing, transparent, titanate nanotubes, mechanical properties, sol-gel

Ice accretion on automobiles, aerospace components, precision instruments, and photovoltaic devices will detrimentally affect their performance and increase the maintenance cost. Despite significant efforts devoted to the investigation of anti-icing coatings in the past decades, mechanically robust and transparent anti-icing coatings have been rarely reported. In this study, titanate nanotubes have been used as filler to prepare mechanically robust anti-icing coatings with a sol-gel method. Specially, the effect of dispersion status of nanitubes on the transmittance, surface roughness and water repellency has been investigated. The optimized smooth, transparent coating exhibits higher water repellency and better anti-icing performance in terms of ice-adhesion strength, icing delay time and ice-nucleation temperature than the rough one. Much higher hardness and scratch resistance than that of commercially available icephobic or anti-icing coatings is obtained on the smooth, transparent sample; the coating also presents good adhesion to the substrate.

1. Introduction

Anti-icing coatings are highly valued for preventing or alleviating adverse consequences of ice accretion on airplanes, marine structures, satellites, weapon systems and energy-harvesting devices. In the past two decades, tremendous efforts have been devoted to the study of anti-icing performance of superhydrophobic coatings inspired by the lotus effect [1] and SLIPS (Slippery Liquid Infused Porous Surface) inspired by *nepenthes*.[2] However, conventional schemes such as creating a roughened surface with trapped air or low-surface-energy liquid in order to enhance water repellency and reduce ice adhesion are not sufficient to produce robust anti-icing coatings.[3] Water repellency at low temperature and suitable mechanical properties are two principal requirements for the future development of anti-icing coatings. To date, the study of mechanical properties of anti-icing coatings has not been widely reported. Among a few available publications, Wang *et al*.[4] reported a superhydrophobic steel surface with anti-icing properties. The surface could withstand a peeling test with 3M adhesive tape and abrasion by 400 grid SiC sandpaper with a scratch length of 110 cm. Chen *et al*.[5] developed an anti-icing coating with a self-lubricating-liquid water layer, the anti-icing layer exhibited low ice-adhesion strength of around 63 ± 11 kPa after ten cycles of an abrasion test with a 10000 mesh sandpaper. However, some of these mechanical abrasion tests were not carried out following any ISO or ASTM standards, so it becomes difficult to compare and evaluate the claimed results. Menini *et al*.[6] deposited a poly (tetrafluoroethylene) (PTFE) coating on aluminum alloys and the surface presented ice-adhesion strength of ~100 kPa with good adhesion to substrate according to the ASTM D3359-02 cross-cut test. Huang *et al*.[7] fabricated an icephobic coating by mixing silica sol and fluorinated acrylate copolymers. The hybrid film exhibited pencil hardness of 4 B and cross-cut adhesion of 0 B. Kimura *et al*.[8] claimed a new icephobic paint with pencil hardness of 2 H. Mazzola [9] reported an aeronautical livery icephobic coating and compared the nanoindentation results of the coating with those for a commercial coating. Both coatings exhibited a hardness of ~150 MPa and

modulus of ~4.8 GPa. Sojoudi *et al.*[10] reported an icephobic bilayer polymer film prepared with initiated chemical vapor deposition (iCVD). The film presented an ice-adhesion strength of ~150 kPa, a hardness of 479.0 ± 7.0 MPa, and elastic modulus of 19.1 ± 1.2 GPa thanks to its dense structure.

Besides mechanical performance, transparency of anti-icing coatings is another essential consideration for applications such as windows, windshields of automobiles, instruments, sensors, cameras, satellites, weapon systems and photovoltaic devices. Although transparency is very important, transparent anti-icing coatings are seldom reported, except for some commercial antifreeze proteins, liquids or agents,[11] however, these coatings are mechanically weak. An earlier study of transparent anti-icing coating was conducted by Kimura *et al.*[8], and one of their reported coatings was water-repellent and transparent. However, it had a mild cream color. Wong *et al.*[2] first fabricated SLIPS, which demonstrated low ice adhesion, and claimed that by choosing a substrate and a lubricant liquid with matching refractive indices, coatings with high transparency could be achieved. Recently, a US patent application (US20180016383A1) revealed a transparent anti-icing coating that contains uniform distribution of particles and asymmetric templates.[12] Although the coating exhibited a kinetic delay of water freezing and depression of an ice melting-point, the ice-adhesion strength of the coating was not reported. To date, fabrication of a transparent anti-icing coating with good mechanical properties remains a challenge. However, due to its great importance for various practical applications discussed above, continued research efforts are expected to be channeled into this area.

Nanosized metal oxides with unique low-dimensionality (0D, 1D, 2D) and physical/electrical properties have recently become a hot topic in various research areas.[13] For instance, TiO_2 nanobelts were well-studied for self-cleaning and anti-fogging applications.[14] In 2014, Tang *et al.*[15] reported for the first time a mechanical force-driven method to grow elongated titanate nanotubes with lengths up to tens of micrometers. Due to

the unique structure of nanotubes, they are able to not only enhance mechanical properties of the coatings, but also provide a perfect site for air trapping or storage of hydrophobic additives. Using low-surface-energy polymers, hydrophobic or superhydrophobic coating with nanotubes can be achieved. Recently, carbon nanotubes were reported in the design of anti-icing coating.[16] In this study, the elongated titanate nanotubes were employed to fabricate anti-icing coatings. One unique feature of this study is application of mechanical stirring during the sol preparation to fabricate coatings with different magnitudes of surface roughness. The effect of surface roughness on light transmittance and anti-icing performance was analysed. Specifically, the anti-icing performance of coated glass slides, including ice-adhesion strength, icing delay time and icing temperature were examined and compared with uncoated glass slides. Furthermore, the resultant coatings were transparent and mechanically strong, thus promising potential applications in aerospace, precision instruments, energy-harvesting devices etc.

2. Results and Discussions

The effect of surface roughness on wetting characteristics of a surface has been studied. It is generally accepted that roughening, or texturing, a hydrophobic surface leads to superhydrophobic surfaces, according to the fundamental wetting theory.[17] In this work, mechanical stirring was employed to change a dispersion state of the nanotube fillers and, as a result, the surface roughness. The transmittance, water wettability, anti-icing performance and mechanical properties of hydrophobic coatings with different surface roughness were investigated.

2.1 Effect of stirring time on surface topology

FESEM and TEM images (**Figure** 1a and 1b) show detailed elongated titanate nanotubes prepared by the hydrothermal reaction. Nanotubes with the lengths up to several tens of micrometres were fabricated and embedded in the sol-gel matrix to obtain hydrophobic coatings as illustrated in **Figure** 1**Figure 1**c. The surface morphology of the prepared titanate nanotube coatings with different stirring times were examined with FESEM (see **Figure** 1d-h). The surfaces were covered with intertwined titanate nanotubes, forming nano-sized pores.

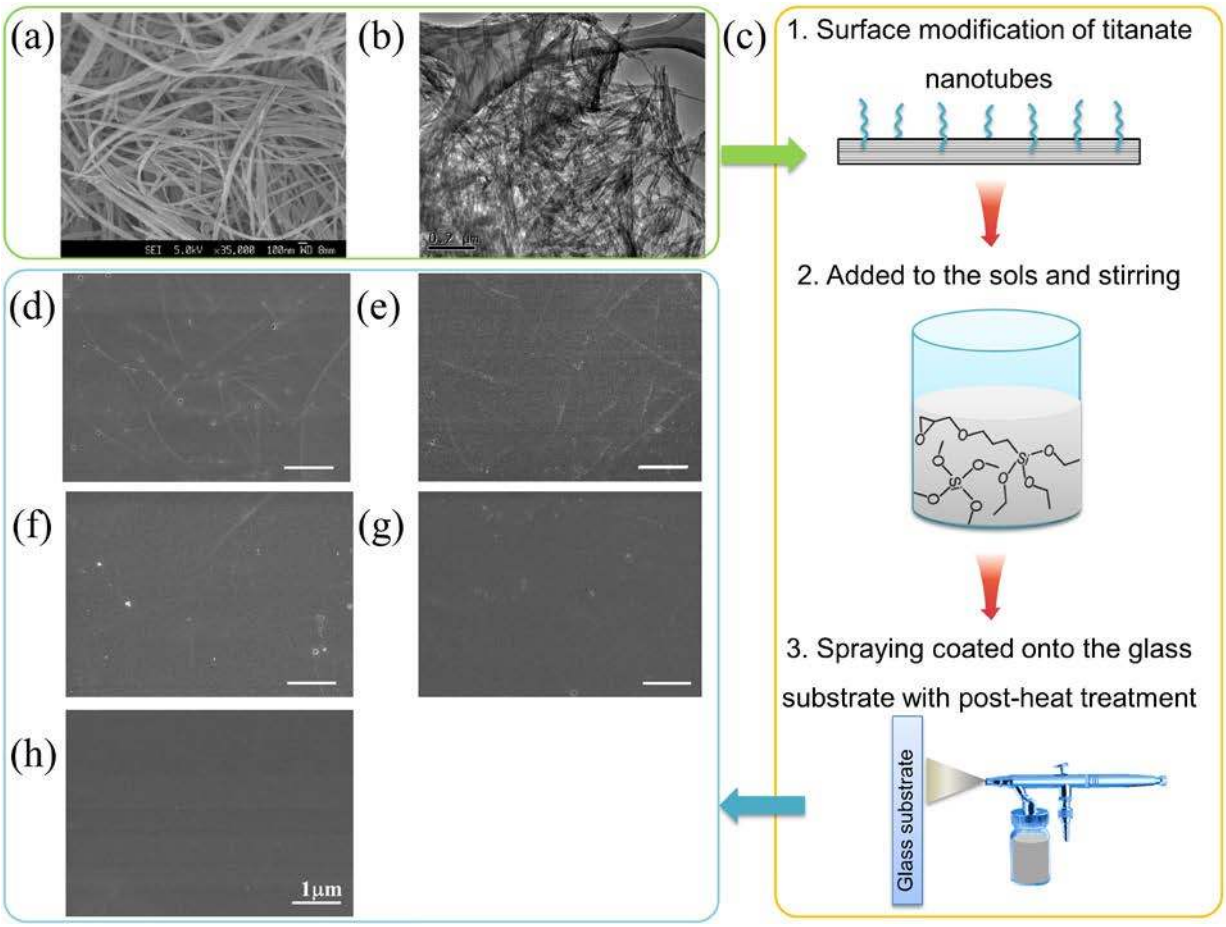

Figure 1. FESEM a) image and TEM b) images of elongated titanate nanotubes; c) schematic illustrations of preparation method of titanate nanotube coatings, and FESEM images of prepared titanate nanotube coatings with different stirring times: d) T_1; e) T_2; f) T_4; g) T_6; h) T_7.

FTIR spectra of the 1-day-stirring (T_1) and the 7-day-stirring (T_7) coatings are shown in **Figure 2**. The two coatings presented exactly the same absorption peaks of Si-O-Si (444 cm^{-1}),[18] Ti-O-Ti (~690 and 582 cm^{-1}),[19] Si-C (~775 cm^{-1}), Si-O (910 cm^{-1}), overlapping Si-O-Si and Si-O-C (broad band in the range of 1000–1,100 cm^{-1}),[18] C-F (1273, 1203 and 1116 cm^{-1}), [20] C-O (1739 cm^{-1}),[21] -CH_3 (2879 and 2940 cm^{-1}),[18] and absorbed water (1641 cm^{-1} and broad band peaked at 3434 cm^{-1}).[22] This is expected since the two coatings are derived from the same precursor.

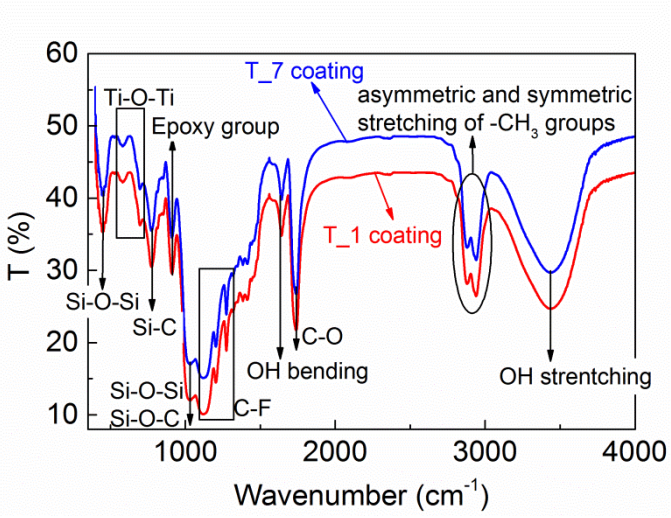

Figure 2. FTIR spectra of the T_1 and T_7 coatings mixed in KBr tablets with weight ratio of 1:20.

AFM images in **Figure** 3 show a clear trend of decreasing surface roughness with the increasing stirring time. The level of surface roughness of T_1 was 365.85 nm, and that for T_7 was 5.66 nm – a reduction by two-orders of magnitude. A decrease in surface roughness with time indicates better dispersion of titanate nanotubes, overcoming agglomeration forces (van der Waals bonding and hydration bonding) in the sol and potentially leading to better mechanical reinforcement and more uniform distribution with low surface energy.

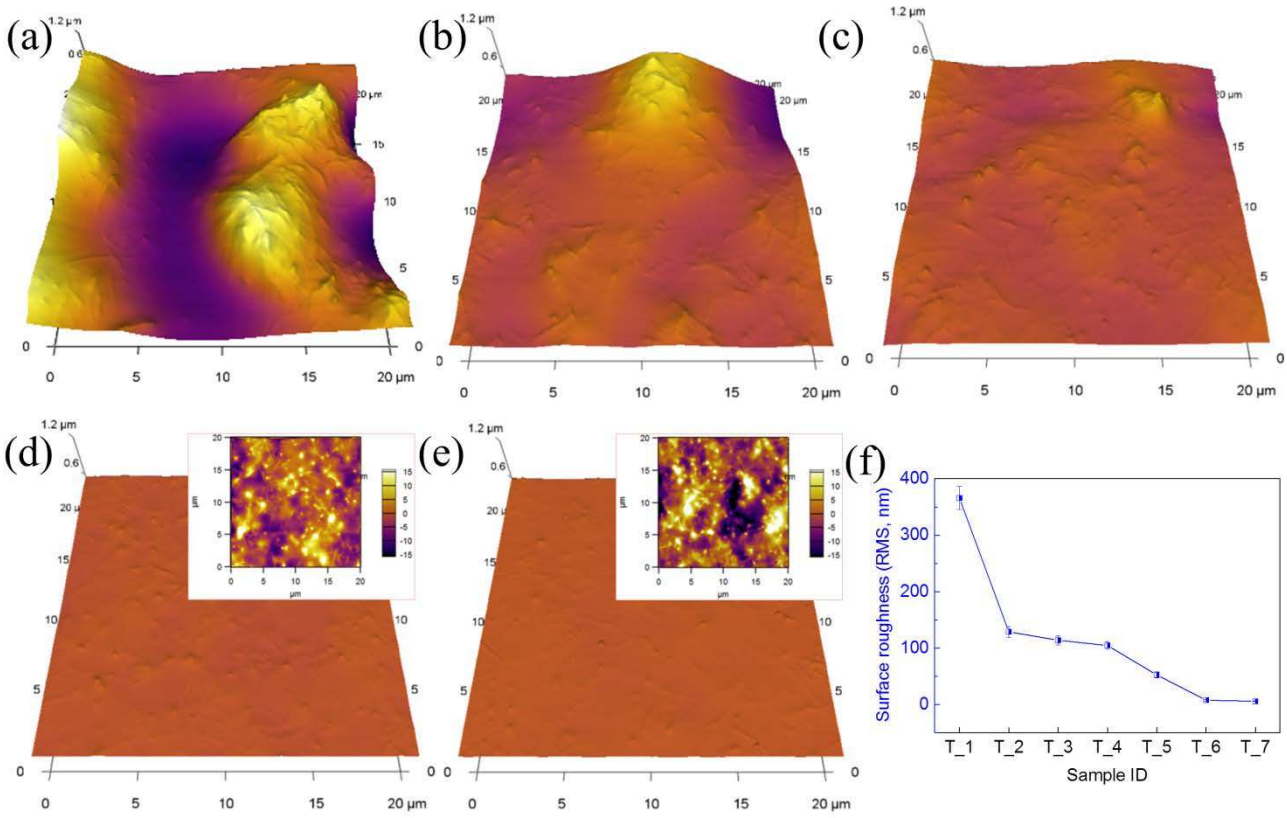

Figure 3. AFM images T_1 a), T_2 b), T_4 c), T_6 d), and T_7 e) samples (the scale bar for these images is 1.2 µm). The inset images of d) and e) show fine features of relatively smooth surfaces (the scale bar is 30 nm). f) Measured root mean square surface roughness of these samples.

To observe clearly dispersion of the filler in the coatings, T_1, T_5, and T_7 samples were examined with TEM (**Figure** 4). The diameter and aspect ratio of the titanate nanotube are about 116 ± 30 nm and 265, repectively.[13c] Titanate nanotubes in the T_1 sample agglomerated into large clusters with sizes of a few micrometers. The flow of the sol in response to the external mechanical force gradually drove the dispersion of nanotubes, and more uniform distributions of them in the coatings are observed in the TEM images of the T_5 and the T_7 samples. Besides the mechanical stirring force, the addition of the low-surface-energy PFOTES, which reacted with -OH groups on nanotube surfaces, significantly

increased the steric or entropic repulsion energy, contributing to dispersion of the nanotubes. Here, mechanical agitation, which is a common method to mix fillers in sols, was for the first time introduced in the sol-gel system to achieve de-agglomeration of nanotubes and obtain coatings with different surface roughness.

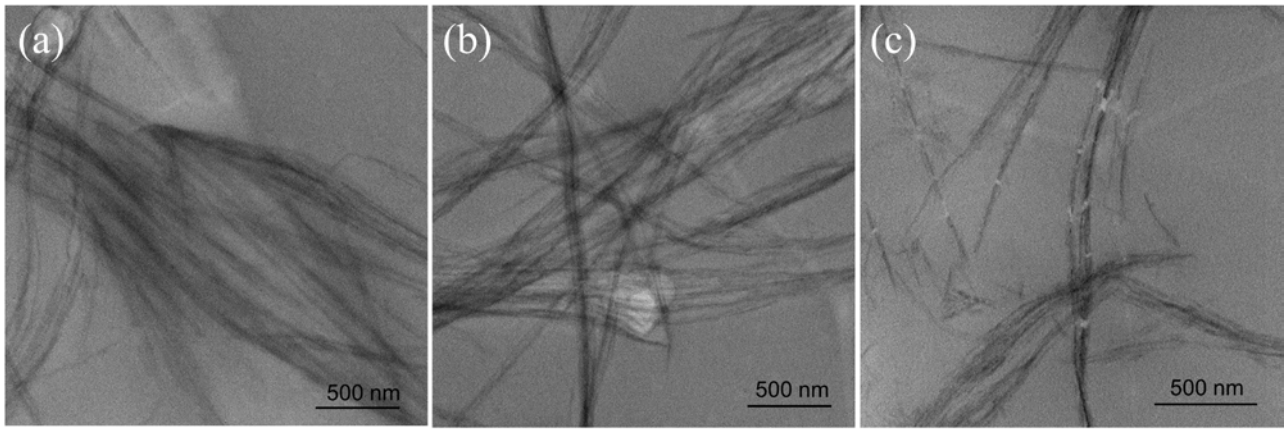

Figure 4. TEM images of T_1 a), T_5 b) and T_7 c) coatings with same amount of titanate nanotubes but different dispersion status.

2.2 Effect of surface roughness on coating transmittance

It is well known that surface unevenness affects transmittance of visible light. Researchers have found that level of agglomeration of the nanoparticles in coatings changed their transmittance.[23] Chang *et al.*[24] reported that increased surface roughness resulted in a decrease in transmittance. In the current work, the extent of transmittance of the coatings increased with the increasing stirring time as shown in the detailed digital images in **Figure** 5a. To investigate the scattering effect of these coatings, digital images were taken employing the setup illustrated schematically in **Figure** 5b; the samples were placed 2 cm away from the coloured logo image. The T_1 sample was translucent, with transmittance lower than 20 %. Continuous stirring led to an increase in the transmittance of samples: the level of transmittance for the T_6 and T_7 samples were comparable to that of uncoated glass. Levels

of transmittance measured with a UV-Vis spectrometer (**Figure** 5c) also confirm the increased transmittance along with increased stirring time. The data for transmittance at the wavelength of 550 nm are plotted against the values of surface roughness in **Figure** 5d: a linear decline can be observed, indicating the dominating influence of surface roughness on transmittance. Thus the decrease in surface roughness led to a significant increase in the transmittance of coatings. In other words, good dispersion of the nanotube clusters reduces significantly the scattering of visible light, resulting in a high transparency of the T_6 and T_7 samples.

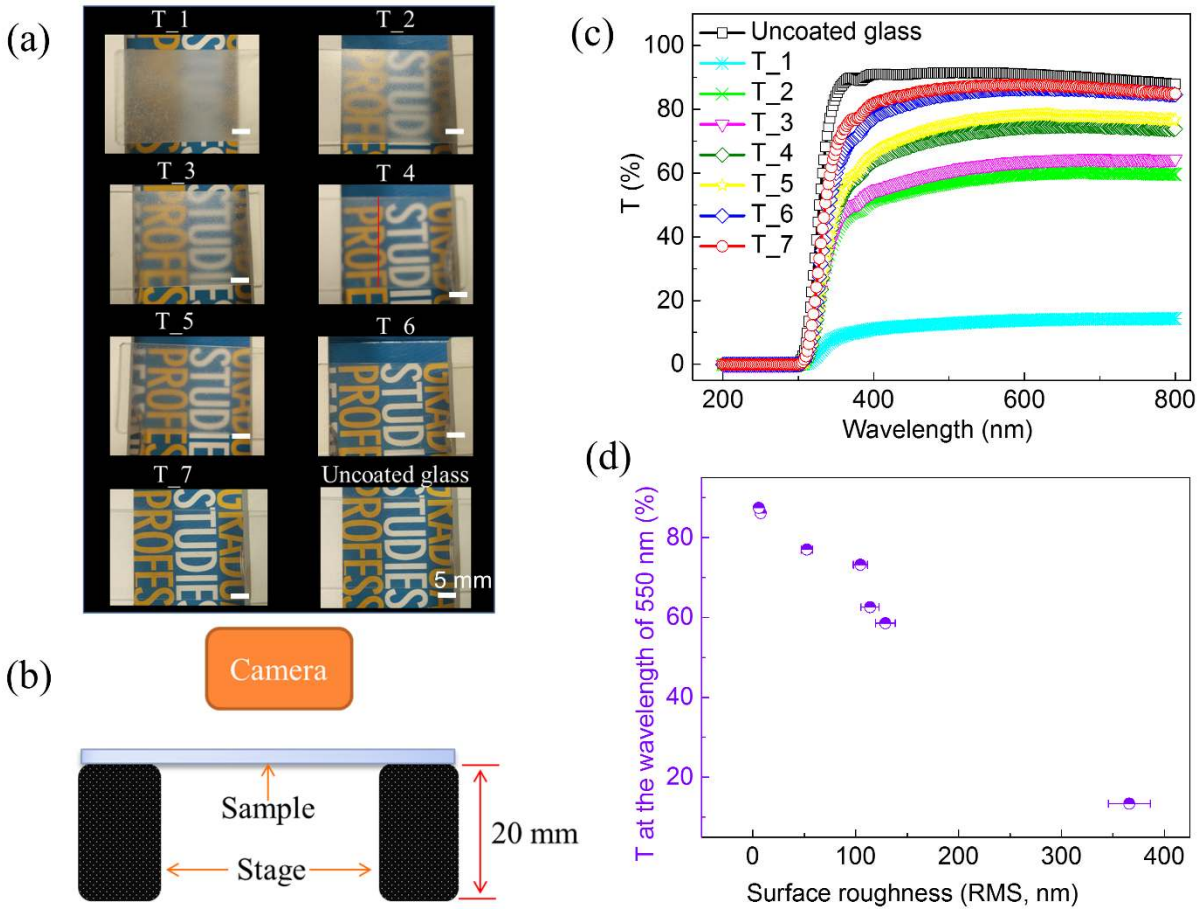

Figure 5. a) Digital images through coated and uncoated glass substrates; b) schematic illustration of test setup; c) transmittance of uncoated and coated with titanate nanotubes coatings glass; d) transmittance of coated glass substrates at wavelength of 550 nm and corresponding surface roughness.

2.3 Water wettability of titanate nanotube coatings

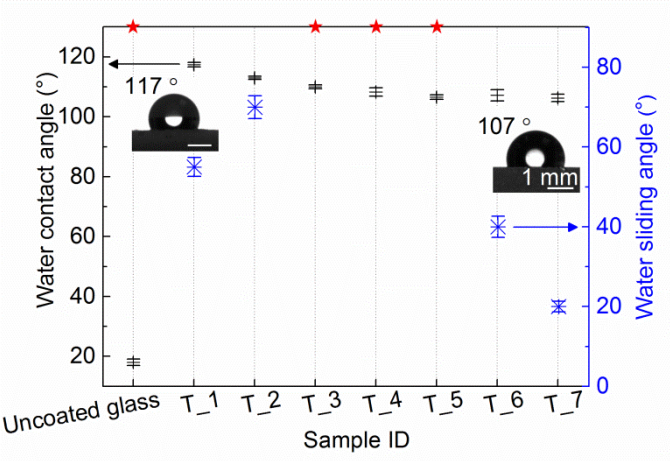

Figure 6. Apparent water contact angles and sliding angles of uncoated glass and titanate nanotube coatings, (insets are microscopic images of water droplets on T_1and T_7 coating surfaces; symbol ★ indicates no sliding even when the plate was tilted by 90°.

A separate study was implemented to assess water wettability of the developed coatings:

Figure 6 shows water contact angles and sliding angles of uncoated glass and the titanate nanotube coatings. The sliding and pinning behaviors of a 10µl droplet on the coating coated glass and uncoated glass can be seen in the Supporting Information Video Clip 1 (played at 8× accelerated speed). Uncoated glass is hydrophilic, exhibiting a low water contact angle with no sliding. The T_1 sample presented the highest water contact angle of around 117° and a sliding angle of 54°. This indicates a likely mixed Cassie-Wenzel state, with some trapped air pockets mixed with complete wetting of the surface asperities. As the stirring time increased, the surface roughness decreased and the contact angle decreased slightly. The mixed wetting condition became more and more dominated by the Wenzel contact, explaining the observed increase in the sliding angle. After 3 days of stirring, the wetting mode is likely to be fully in the Wenzel regime, and water droplet could not roll off by its gravity force, even when the substrate was titled by 90°. With a further increase in the stirring time, the surface

became very smooth; under such condition the water adhesion becomes dependent on the surface energy only. The water droplet could slide off and the sliding angle decreased with increased smoothness. The sliding behavior on the T_6 and the T_7 samples can be explained by the interfacial slippage between the water droplet and the coating surface.[3c] Based on our studies, it can be concluded that for a hydrophobic coating, surface topology dominates the sliding behavior, or water repellency, of coatings. In particular, the T_7 sample exhibited a water contact angle of 107° and the lowest sliding angle at 20°, presenting good water-repellent properties.

2.4 Anti-icing performance of titanate nanotube coatings

The wettability tests were followed by analysis of anti-icing performance; **Figure** 7a demonstrates the measured ice-adhesion strength with the coated and uncoated glass substrates at -15 °C and -20 °C. Compared to an uncoated glass, three-fold lower ice-adhesion strength was measured for the titanate nanotube coatings.

The ice-adhesion strengths of these coatings fell into the range of 57 ~ 87 kPa, below a well-accepted threshold value of 100 kPa for icephobic coatings.[3c, 25] These levels of adhesion strength are only around half of the reported ice adhesion strength on carbon-nanotube reinforced polymer composites.[26] Although the surface roughness of titanate nanotube coatings varies greatly depending on the stirring time, only a slight change in the ice-adhesion strength was observed. Researchers in the past attempted to establish a relationship between the ice-adhesion strength and the water contact angle or the work of adhesion with water,[27] however, the surface energies of the tested surfaces were not kept the same. Here, the apparent surface energy, apparent water contact angle and ice-adhesion strength of samples are compared in **Figure** 7b. It was found that the apparent surface energy and ice-adhesion strength presented a similar trend, significantly different from that for the apparent water contact angle, implying a strong influence of the surface energy on the ice-

adhesion strength of samples. Menini and Farzaneh[28] defined four factors that affected the ice-adhesion strength: (i) intermolecular forces (such as covalent, electrostatic and van der Waals forces); (ii) mechanical-interlocking-induced adhesion; (iii) diffusion and (iv) the presence of a liquid-like layer at the ice–substrate interface. In this study, due to the mountain-valley type structure of titanate nanotube coatings, no significant mechanical interlocking was observed. The low surface energies of these coatings allowed lower intermolecular forces and lower diffusion, resulting in low ice-adhesion strength. It is noticed that both the T_1 and T_7 samples presented the lowest ice–adhesion strength; however, due to their greatly different surface roughness, they may present different mechanisms of ice adhesion. The low ice-adhesion strength of the T_1 surface was mainly due to partial wetting, allowing air-trapping inside the coatings. Once iced formed, the trapped air could serve as an initial interfacial crack at the ice-solid interface, reducing the energy of separation.[29] On the other hand, the reason for the low ice-adhesion strength of the T_7 surface primarily lies in the low contact-angle hysteresis on smooth surfaces thus allowing minimal contact-line pinning.[30] In particular, nearly no change in the ice-adhesion strength of the T_7 sample was observed at different temperatures after testing for more than five times, indicating its good anti-icing reliability.

The icing-delay times of the uncoated glass, the T_1, and the T_7 samples at -15 °C are shown in **Figure** 7c. It took 3 min and 17 sec for the temperature of all the samples to reach -15 °C. The droplet on the uncoated glass surface started to freeze first after 54 s, followed by the T_1 sample (173 s). The longest icing delay time was observed on the T_7 sample, which was nearly 6 min.

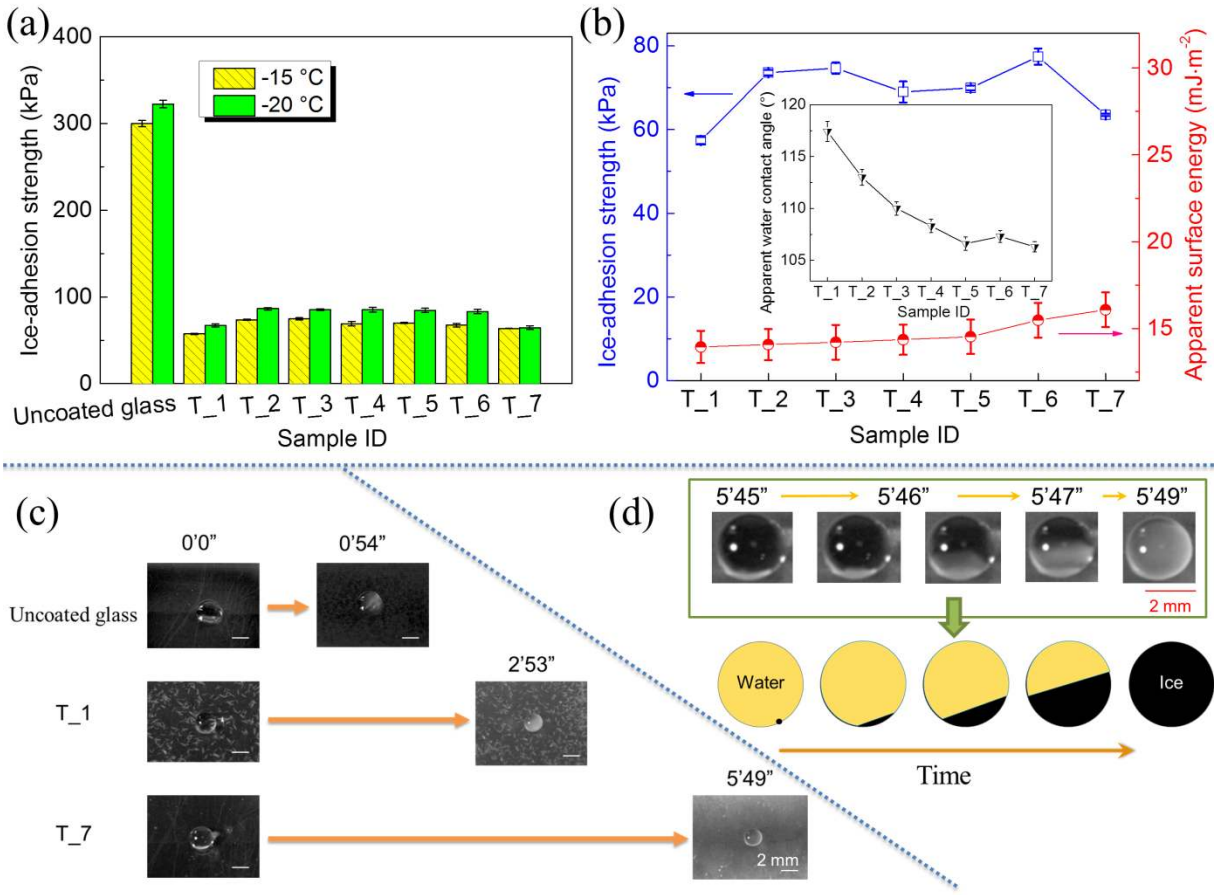

Figure 7. a) Ice-adhesion strength of coated and uncoated glass at -15 °C and -20 °C, b) comparison of measured ice-adhesion strengths and apparent surface energies of titanate nanotube coatings (insets shows apparent water contact angles); c) icing-delay times of the uncoated glass, T_1, and the T_7 samples at -15 °C; d) time-sequential digital images captured with a high-speed camera during icing-delay test and schematic illustration of ice growth on water-solid interface.

During the icing-delay test, ice nucleation on the three-phase contact line was observed regardless of the surface roughness (see Supporting Information Video Clip 2, Frame rate per second: 28.6). **Figure** 7d provides the time-sequential digital images captured with a high-speed camera during the icing-delay test and illustrated the ice-growing process on the water-solid interface. This result is consistent with previous reports,[31], demonstrating that

heterogeneous nucleation along a three-phase contact line is a preferred option as compared to the solid-liquid interface.

To further study the anti-icing performance, the icing temperature of the T_1 and T_7 samples was measured and compared with that of the uncoated sample; **Figure** 8a shows the results for icing temperatures tested for 500 cycles. Statistical analysis of heterogeneous nucleation behavior of supercooled water droplets on these samples according to our previous report.[31a] is given in **Figure** 8b-h. The distribution of icing temperatures was plotted by binning the measured data with a bin width of 0.2 °C. The resulted freezing distributions of each sample as a function of the temperature are shown in **Figure** 8b-d and fitted with the Gauss equation. The Gause peak temperature for the maximum freezing events for each sample are shown in **Figure** 8f. The freezing probability can be defined as Equation (1)

$$P = \frac{N_i}{N_0}, \tag{1}$$

where N_i is the freezing event in the i_{th} bin and N_0 is the total number of icing events (500 in the current study). The corresponding temperature-survival curve defined as $F(t)$[32] was employed to analyze the freezing probability distributions as shown in Equation (2):

$$F(t) = \frac{N(t)}{N_0}, \tag{2}$$

where $N(t)$ is the unfrozen events at temperature *t*; the obtained results are shown in **Figure**. 8e. In some reports, the temperature $t_{0.5}$, at which $F(t) = 0.5$, was used as the ice-nucleation temperature. A comparison of the Gauss peak temperatures obtained from **Figure** 8b-d and $t_{0.5}$ shown in **Figure** 8e demonstrate their perfect agreement (**Figure** 8f). The average values of the icing temperature of the uncoated glass, the T_1, and the T_7 samples were -21.9 ± 0.5 °C, -25.0 ± 0.6 °C and -25.8 ± 0.5 °C, respectively. Compared to the icing temperature of the uncoated glass, a large decrease was clearly identified for the T_1 and the T_7 samples.

Additionally, the line ice-nucleation rate $R_S{}^*(T_i)$ of the uncoated glass, T_1 and T_7 samples was investigated based on the above freezing probability distributions as shown in

Equation (3). The statistical nucleation rate $R(T_i)$ at T_i was binned with a width of ΔT_i, which contains n_i freezing events, then

$$R(T_i) = \frac{cn_i}{\Delta T_i\left(\frac{n_i}{2}+\sum_{j>i} n_j\right)} \ , \tag{3}$$

where c is the cooling rate (5 °C/min in our experiment), $\sum_{j>i} n_j$ is the sum of unfrozen icing events. The corresponding line nucleation rate can be expressed as Equation (4):

$$R_S{}^*(T_i) = \frac{R(T_i)}{S} \ , \tag{4}$$

where S is the three-phase contact-line length between the water droplet and the coating surface (schematically illustrated in **Figure** 8g). It can be calculated as $S = 2\pi r$, where

$$r = \left[\frac{3V}{\pi(2-3\cos\theta+\cos^3\theta)}\right]^{1/3} \sin\theta \ , \tag{5}$$

and V is the volume of the water droplet, θ is the apparent contact angle.[33] The corresponding values of θ, r and S for the uncoated glass, T_1 and T_7 samples are shown in **Figure** 8g. Consequently, the calculated $R_S{}^*(T_i)$ for these coatings according to Equation (5) are shown in **Figure** 8h. At any given temperature, the T_7 sample presented the lowest line ice-nucleation rate, followed by the T_1 sample; both are significantly lower than that of the uncoated glass.

It is believed that heterogeneous ice nucleation occurs more easily on rough surfaces than on flat ones, since the site adsorption and clustering mechanism are rendered less effective when the surface is flat.[34] The T_7 sample is neatly flat, while the T_1 sample is rough; as a result, the T_7 sample presented a lower icing temperature than the T_1 sample. Although the uncoated glass shares similar surface roughness with the T_7 sample, because of its hydrophilic property and high surface energy, a much higher icing temperature than for the T_7 sample is expected.

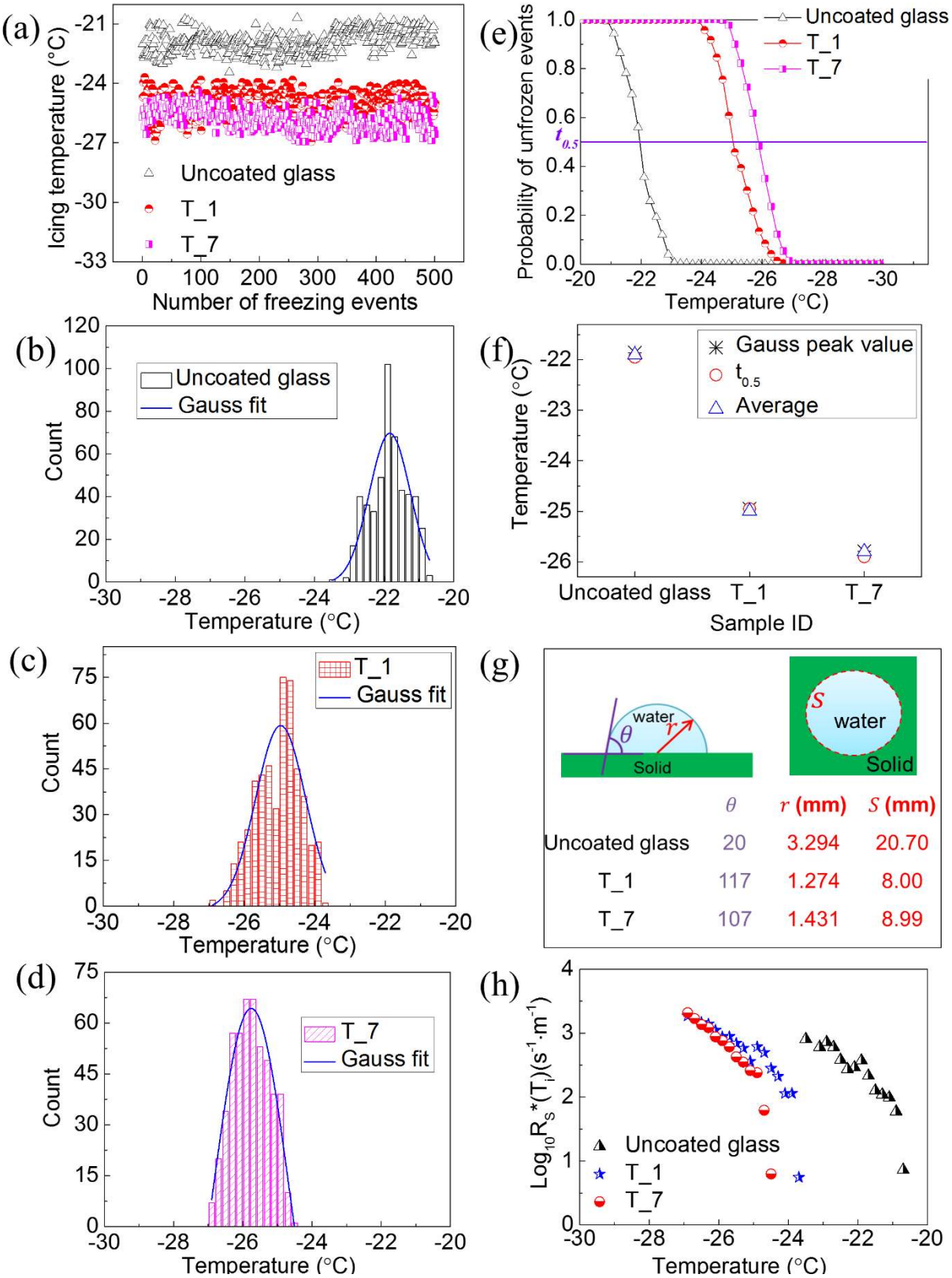

Figure 8. a) Ice-nucleation temperature of T_1, T_7 sample and uncoated glass; b) histogram of freezing events on uncoated glass, T_1 c) and T_7 d) samples with bin width of 0.2 °C; e) temperature-survival curves of uncoated glass, T_1 and T_7 samples; f) schematic illustration

of water contact angle and corresponding radius and length of three-phase contact line with calculated values for uncoated glass, T_1, and T_7 samples; g) the line-nucleation rate of the uncoated glass, T_1 and T_7 samples.

Even though the ice-adhesion strength of all the samples depends less on surface roughness, the icing-delay time and ice-nucleation temperature are affected significantly by surface roughness. The low ice-nucleation temperature and the delayed icing-time of a water droplet on the T_7 sample are important indicators for its anti-icing performance.

2.5 Mechanical properties of titanate nanotube coatings

A major weakness of many existing anti-icing coatings is their poor mechanical performance, which hinders their practical applications. In this work, hardness, scratch resistance and adhesive properties of the titanate nanotube coatings were investigated according to the ASTM standard. The values of hardness and the elastic modulus of the studied titanate nanotube coatings measured with nano-indentation are given in **Figure** 9a. An upward trend clearly identifies the increase in hardness and the elasticity modulus of the coatings with the increased stirring time. This is in line with other reports that higher coating roughness and porosity lead to lower values of hardness and modulus.[35] The T_7 sample demonstrated hardness of 380 ± 10 MPa and the elastic modulus of 12.39 ± 0.46 GPa; these are comparable with the values of iCVD film [10] and higher than aeronautical livery icephobic coating [9]. We believe that the excellent mechanical properties are due to 1) better dispersion of nanotubes throughout the coating, and 2) better mechanical reinforcement using a nanotube structure.

Scratch resistance of the T_1 and the T_7 samples and microscopic images of samples after scratching are compared in **Figure** 9b and 8c. The rough T_1 sample exhibited pencil-scratch resistance of 4 H, while the smooth T_7 sample presented 5 H (the pencil-hardness scale

ranges from 6 B for the softest pencil up to 9 H for the hardest), which is significantly higher than the reported icephobic paint[8] and copolymer hybrid film[7]. These results follow the trend of the nano-indentation results. Since the T_1 sample was rough, graphite fragments were left on the coating surface, while nearly no residue was found on the smooth T_7 coating surface. In addition, the T_1and T_7 samples demonstrated a similar cross-cut adhesion grade at 4 B (**Figure** 9d and 9e), indicating strong adhesion to the substrate. Mechanical studies of the T_7 sample verified its superior mechanical properties compared to the currently reported anti-icing or icephobic coatings.[6-9, 36]

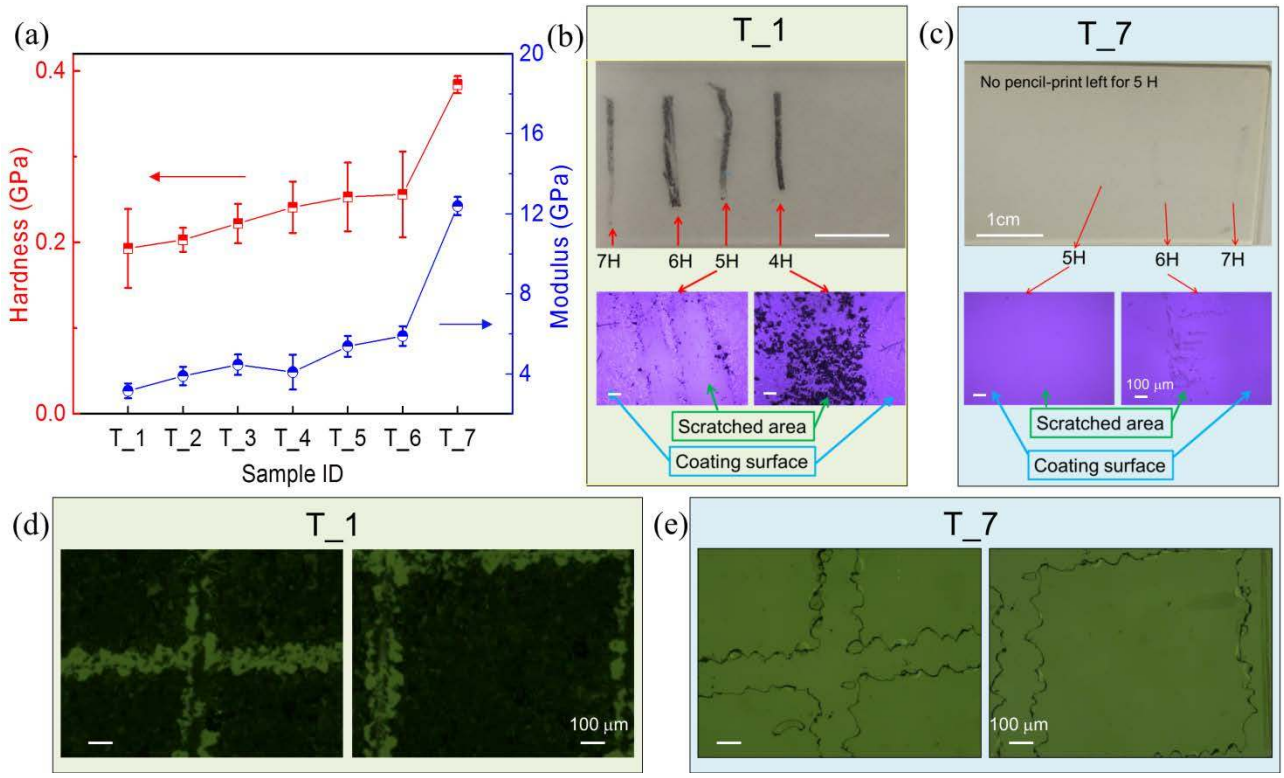

Figure 9. a) Hardness and elastic modulus of titanate nanotube coatings measured with nano-indentation. Research of pencil-scratch test and microscopic observation for T_1 b) and T_7 c) samples and cross-cut tape adhesion test for T_1 d) and T_7 e) samples.

Ooptically transparent anti-icing coatings are useful for a wide range of applications where optical transmission is critical, such as solar panels, windows of a house or optical devices,

windshield of automobiles, as well as for cases where aesthetic value of the protected objects need to be preserved, such airplanes, wind turbines, and sports facilities and so on. With a transparent coating, the original color of protected objects will not be altered either for aesthetic reasons or due to functional requirements. Together with a higher transmittance, mechanical robustness and good anti-icing performance, the T_7 sample has a very promising prospective for practically applications in cold regions.

3. Conclusions

A transparent anti-icing coating was fabricated employing the elongated titanate nanotubes with a sol-gel method. The coating exhibited good water repellency and anti-icing properties. A significant reduction in the ice-adhesion strength and ice-nucleation temperature was observed. The effect of surface roughness on transparency, water wettability, and icephobicity was also investigated. Although little influence of surface roughness on the ice-adhesion strength was observed, there appears to be a strong effect of surface roughness on the ice-nucleation process. Our observations confirm ice nucleation along the three-phase contact line regardless of the surface roughness. The produced transparent anti-icing coating demonstrated good hardness and pencil-scratch resistance, as well as excellent adhesion to glass substrates. This mechanically robust anti-icing coating opens a new avenue towards smooth solid coatings for applications in windows, windshields of automobiles, energy-harvesting devices, and aerospace components.

4. Experimental Section

4.1 Materials

Titanium oxide nanopowder (AEROXIDE® TiO_2 P25) was obtained from Evonik Industries. Sodium hydroxide pellets, silicone oil, 1H, 1H, 2H, 2H-perfluorooctyltriethoxysilane (PFOTES), 3-glycidoxypropyltrimethoxysilane (GLYMO),

itaconic acid and tetraethylorthosilicate (TEOS), ethylene glycerol and diiodomethane were purchased from Sigma Aldrich. Microscope glass slides and cover glass (used for ice-nucleation temperature tests) used as substrates were obtained from Sailboat Lab Co., Ltd. and Marienfeld, respectively.

4.2 Methods

4.2.1 Fabrication of titanate nanotubes

A process of preparation of titanate nanotubes followed the same procedure as reported before.[15] 0.1g titanium oxide nanopowders were ultrasonically mixed with 10 M sodium hydroxide and stirring magnetically for 24 hours, and then transferred to a hydrothermal autoclave, soaked in silicon oil bath and heated at 130 °C for 24 hours with continuous magnetic stirring. The reaction product was washed with deionized (DI) water and centrifuged for 2-3 times until the pH value of the particle suspension solution was around 8. Ultralong sodium titanate nanotubes were obtained, and used as coating fillers.

4.2.2 Fabrication of anti-icing coatings

The resultant titanate nanotubes were dispersed in 10 ml methanol and modified with 5 ml of 1wt. % PFOTES solution. The preparation of PFOTES solution was based on our previous report[37]. The above solution was magnetically stirred for 24 hours, then 0.004 mol TEOS, 0.038 mol DI water, and 0.02 mol GLYMO were added. Itaconic acid was used to acidify the sol to pH 4~5. The sol was first placed in an ultrasonic bath for 30 min, and then magnetically stirred at 500 rpm for different numbers of days until a transparent coating was obtained. The prepared sols were spray-coated onto the glass slides using an airbrush kit (AS06KB) with a 1.5 mm diameter nozzle under compressed air (at pressure of 345 kPa). A distance between the airbrush and the substrate was kept at 8 cm. The airbrush was moved laterally back and forth until a uniform coating was deposited. Finally, the prepared samples were cured in an

oven at 110 °C for 1.5 hours. The weight percentage of titanate nanotubes in the final coating is ~2.3 wt.%., and the thickness of the final coating is around 30 µm. The resultant coatings were denoted T_1, T_2, T_3, T_4, T_5, T_6 and T_7, the digit represents the number of days during the magnetic stirring of the sols.

4.3 Characterization

Surface microstructures of the obtained coatings were examined with a field emission scanning electron microscopy (FESEM, JSM-6360, Japan) and atomic force microscopy (AFM, Asylum Research Cypher S, USA). The surface roughness (root mean square, RMS) of coatings was recorded from the AFM measurement. The scanning area was 20 µm × 20 µm. The roughness values were averaged from at least five measurements obtained at different locations of the coatings. FTIR spectra of coatings were scanned with Magna 550 Fourier transform infrared (FTIR) spectrometer (ATR-FTIR, Perkin-Elmer Inc.). The tested coatings were scratched down from the applied substrate and mixed in KBr powders with a weight ratio of 1:20. Then the mixed powders were compressed into a tablet with a diameter of 10 mm. Transmission electron microscopy (TEM, JEOL 2100 HR, Japan) operating at 200 kV was used to observe the distribution of nanoparticles in the coatings. The transmittance of the coatings was examined by UV-VIS spectrophotometer (Shimadzu UV-2501PC, Japan). Water contact angles and sliding angles were measured with a contact angle system (OCA 20, Dataphysics Co., Germany). Surface energies of coatings were measured following the Owens, Wendt, Rabel and Kalble (OWRK) method[38], in which DI water and ethylene glycerol were used as polar liquids, and diiodomethane was used as a non-polar liquid. The icing delay time was measured at -15 °C on a cooling stage of the contact-angle measurement system. The glass-substrate samples were directly placed on the cooling stage. A 10 µl water droplet was dropped on to sample surface, then the temperature was cooled down and held at -

15 °C. The process of ice nucleation and growth on the water-solid interface was recorded with a high-speed video camera (Phantom Micro 120). The icing delay time of the coating was determined by the time, at which the light reflection of the water droplets suddenly changed from clear and reflective to blurry and non-transparent.

Measurements of ice-adhesion strength between an ice block and coating surfaces followed the scheme from our group's previous report[39]. In brief, a Teflon mold filled with DI water was covered with a coated substrate on top, and then the whole setup was placed up-side down and stored in a climate chamber (Cincinnati Sub-Zero environmental chambers, USA) for 24 hours at -20 °C. The ice-nucleation temperature of coatings was studied using the previously reported home-designed automatic ice nucleation measurement system[40]. The system utilizes a laser beam and an optical detector to record the freezing events. In this experiment, a 10 µl DI water droplet was placed on the coating surface, and then cooled down from 22 °C to -30 °C. The ramp rate from 22 °C to 0 °C was set at 40 °C/min, while the ramp rate from 0 °C to -30 °C was set as 5 °C/min. Once the whole cycle was completed, the iced droplet was warmed up to 22 °C and held for 2 min to ensure a complete melting of the ice droplet before the next cycle began. Icing temperatures of 500 cycles for each water droplet were recorded and statistically analyzed.

A pencil-scratch test was made using a commercial pencil-scratch tester (Scratch Hardness Tester Model 291, ERICHSEN) according to ASTM D3363 standard. The coating quality was measured by cross-cut adhesion test, which was based on the ASTM D3359 standard. After cross cutting, the coatings were examined under an optical microscope (Olympus BX51). The elastic modulus and hardness of the coatings were measured using a nano-indentator (Nano-Indentation & Micro-Scratch System, Wrexham, United Kingdom). Readings were made at indentation depth from 1800 to 2000 nm. For each specimen, 15 points (in 3 lines, 5 points for each line) were tested.

Supporting Information
Supporting Information Video Clip 1 is available from the Wiley Online Library or from the author.

Acknowledgements

This work was supported by Nanyang Technological University in form of a research scholarship, and the Agency for Science, Technology and Research (A*STAR) of Singapore [SERC 1528000048].

References

1. T. Maitra; S. Jung; M. E. Giger; V. Kandrical; T. Ruesch; D. Poulikakos, *Adv. Mater. Interfaces* **2015,** *2* (16).

2. T. S. Wong; S. H. Kang; S. K. Tang; E. J. Smythe; B. D. Hatton; A. Grinthal; J. Aizenberg, *Nature* **2011,** *477* (7365), 443-447.

3. a) M. J. Kreder; J. Alvarenga; P. Kim; J. Aizenberg, *Nat. Rev. Mater.* **2016,** *1*, 15003; b) T. Furuta; M. Sakai; T. Isobe; A. Nakajima, *Langmuir* **2010,** *26* (16), 13305-13309; c) K. Golovin; S. P. Kobaku; D. H. Lee; E. T. DiLoreto; J. M. Mabry; A. Tuteja, *Sci. Adv.* **2016,** *2* (3), e1501496; d) X. Wu; S. Zheng; D. A. Bellido-Aguilar; V. V. Silberschmidt; Z. Chen, *Mater. Des.* **2018,** *140*, 516-523.

4. N. Wang; D. Xiong; Y. Deng; Y. Shi; K. Wang, *ACS Appl. Mater. Interfaces* **2015,** *7* (11), 6260-6272.

5. J. Chen; R. Dou; D. Cui; Q. Zhang; Y. Zhang; F. Xu; X. Zhou; J. Wang; Y. Song; L. Jiang, *ACS Appl. Mater. Interfaces* **2013,** *5* (10), 4026-4030.

6. R. Menini; Z. Ghalmi; M. Farzaneh, *Cold Reg Sci Technol.* **2011,** *65* (1), 65-69.

7. Y. Huang; M. Hu; S. Yi; X. Liu; H. Li; C. Huang; Y. Luo; Y. Li, *Thin Solid Films* **2012,** *520* (17), 5644-5651.

8. S. Kimura, Y. Yamagishi, A. Sakabe, T. Adachi, M. Shimanuki, SAE Technical Paper 2001-01-3315 2007, 9.

9. L. Mazzola, *Surface Engineering* **2016,** *32* (10), 733-744.

10. H. Sojoudi; G. H. McKinley; K. K. Gleason, *Mater Horiz.* **2015,** *2* (1), 91-99.

11. C. Antonini; M. Innocenti; T. Horn; M. Marengo; A. Amirfazli, *Cold Reg Sci Technol.* **2011,** *67* (1), 58-67.

12. A. F. Gross, A. P. Nowak, inventors; HRL Laboratories LLC, assignee. *United States patent application* **2018,** US 15/718,181.

13. a) Y. Tang; Y. Zhang; X. Rui; D. Qi; Y. Luo; W. R. Leow; S. Chen; J. Guo; J. Wei; W. Li, *Adv. Mater.* **2016,** *28* (8), 1567-1576; b) Y. Zhang; O. I. Malyi; Y. Tang; J. Wei; Z. Zhu; H. Xia; W. Li; J. Guo; X. Zhou; Z. Chen, *Angew. Chem.* **2017,** *129* (47), 15043-15048; c) Y. Tang; Y. Zhang; J. Deng; D. Qi; W. R. Leow; J. Wei; S. Yin; Z. Dong; R. Yazami; Z. Chen, *Angew. Chem. Int. Ed.* **2014,** *53* (49), 13488-13492.

14. Y. Lai; Y. Tang; J. Gong; D. Gong; L. Chi; C. Lin; Z. Chen, *J. Mater. Chem.* **2012,** *22* (15), 7420-7426.

15. Y. Tang; Y. Zhang; J. Deng; J. Wei; H. L. Tam; B. K. Chandran; Z. Dong; Z. Chen; X. Chen, *Adv. Mater.* **2014,** *26* (35), 6111-6118.

16. a) L. Zheng; Z. Li; S. Bourdo; K. R. Khedir; M. P. Asar; C. C. Ryerson; A. S. Biris, *Langmuir* **2011,** *27* (16), 9936-9943; b) O. Gohardani; M. C. Elola; C. Elizetxea, *Prog. Aerosp. Sci* **2014,** *70*, 42-68.

17. A. Cassie; S. Baxter, *J. Chem. Soc. Faraday Trans.* **1944,** *40*, 546-551.

18. S. Amoriello; A. Bianco; L. Eusebio; P. Gronchi, *J. Sol-Gel Sci. Technol.* **2011,** *58* (1), 209-217.

19. a) H. Zhang; X. Lv; Y. Li; Y. Wang; J. Li, *ACS nano* **2009,** *4* (1), 380-386; b) H. Zuo; J. Sun; K. Deng; R. Su; F. Wei; D. Wang, *Chem. Eng.Technol.* **2007,** *30* (5), 577-582.

20. S. Pazokifard; S. M. Mirabedini; M. Esfandeh; S. Farrokhpay, *Chemeca 2011: Engineering a Better World: Sydney Hilton Hotel, NSW, Australia, 18-21 September 2011* **2011**, 2155.

21. P. Innocenzi; A. Martucci; M. Guglielmi; L. Armelao; S. Pelli; G. Righini; G. Battaglin, *J. Non-Cryst. Solids* **1999,** *259* (1-3), 182-190.

22. E. Lataste; A. Demourgues; H. Leclerc; J.-M. Goupil; A. Vimont; E. Durand; C. Labrugère; H. Benalla; A. Tressaud, *J. Phys. Chem. C* **2008,** *112* (29), 10943-10951.

23. a) B. J. Basu; J. Manasa, *J. Colloid Interface Sci.* **2011,** *363* (2), 655-662; b) M. Hikita; K. Tanaka; T. Nakamura; T. Kajiyama; A. Takahara, *Langmuir* **2005,** *21* (16), 7299-7302; c) R.Kasemann; H.Schmidt, *New J. Chem.* **1994,** *8*, 1117-1123.

24. K. C. Chang; Y. K. Chen; H. Chen, *J. Appl. Polym. Sci.* **2008,** *107* (3), 1530-1538.

25. V. Hejazi; K. Sobolev; M. Nosonovsky, *Sci. Rep.* **2013,** *3*.

26. a) O. Gohardani; D. W. Hammond, *Cold Reg Sci Technol.* **2013,** *96*, 8-16; b) Y. Wang; J. Xue; Q. Wang; Q. Chen; J. Ding, *ACS Appl. Mater. Interfaces* **2013,** *5* (8), 3370-3381.

27. a) A. Dotan; H. Dodiuk; C. Laforte; S. Kenig, *J Adhes Sci Technol.* **2009,** *23* (15), 1907-1915; b) A. J. Meuler; J. D. Smith; K. K. Varanasi; J. M. Mabry; G. H. McKinley; R. E. Cohen, *ACS Appl. Mater. Interfaces* **2010,** *2* (11), 3100-3110; c) Y. H. Yeong; J. Sokhey; E. Loth, Advances in Polymer Science, Spinger, Berlin, Germany, **2017,** 1-23.

28. R. Menini; M. Farzaneh, *J. Adhes. Sci. Technol.* **2011,** *25* (9), 971-992.

29. M. Nosonovsky; V. Hejazi, *Acs Nano* **2012,** *6* (10), 8488-8491.

30. H. A. Stone, *ACS Nano* **2012,** *6* (8), 6536-6540.

31. a) Q. T. Fu; E. J. Liu; P. Wilson; Z. Chen, *Phys. Chem. Chem. Phys.* **2015,** *17* (33), 21492-21500; b) S. Suzuki; A. Nakajima; N. Yoshida; M. Sakai; A. Hashimoto; Y. Kameshima; K. Okada, *Chem. Phys. Lett.* **2007,** *445* (1), 37-41; c) C. W. Gurganus; J. C. Charnawskas; A. B. Kostinski; R. A. Shaw, *Phys. Rev. Lett.* **2014,** *113* (23), 235701..

32. P. Wilson; A. Heneghan; A. Haymet, *Cryobiology* **2003,** *46* (1), 88-98.

33. P. Hao; C. Lv; X. Zhang, *Appl. Phys. Lett.* **2014,** *104* (16), 161609.

34. D. Bassett; E. Boucher; A. Zettlemoyer, *J. Colloid Interface Sci* **1970,** *34* (3), 436-446.

35. a) C. C. Gonzaga; P. F. Cesar; C. Y. Okada; C. Fredericci; F. Beneduce Neto; H. N. Yoshimura, *Mater. Res.* **2008,** *11* (3), 301-306; b) O. Sarikaya, *Surf. Coat. Technol.* **2005,** *190* (2), 388-393; c) Q. Yang; T. Senda; A. Ohmori, *Wear* **2003,** *254* (1), 23-34.

36. R. Menini; M. Farzaneh, *Surf. Coat. Technol.* **2009,** *203* (14), 1941-1946.

37. X. Wu; Q. Fu; D. Kumar; J. W. C. Ho; P. Kanhere; H. Zhou; Z. Chen, *Mater. Des.* **2016,** *89*, 1302-1309.

38. a) D. K. Owens; R. Wendt, *J. Appl. Polym. Sci* **1969,** *13* (8), 1741-1747; b) D. Kaelble, *J. Adhes. Adhes.* **1970,** *2* (2), 66-81; c) W. Rabel, *Farbe und Lack* **1971,** *77*, 997-1006.

39. Q. Fu; X. Wu; D. Kumar; J. W. Ho; P. D. Kanhere; N. Srikanth; E. Liu; P. Wilson; Z. Chen, *ACS Appl. Mater. Interfaces* **2014,** *6* (23), 20685-20692.

40. a) T. Verho; C. Bower; P. Andrew; S. Franssila; O. Ikkala; R. H. A. Ras, *Adv. Mater.* **2011,** *23*, 673-678; b) P. Judeinstein; C. Sanchez, *J. Mater. Chem.* **1996,** *6* (4), 511-525.

Dispersion status of elongated titanate nanotubes in sols is investigated. By applying mechanical force for different duration, coatings with different transmittance and water repellency are obtained. Comparison of coatings with distinct dispersion status of nanotubes verifies that coatings with uniform dispersion of nanotubes exhibit better anti-icing performance than those with aggregated ones.

Keyword anti-icing, transparent, titanate nanotubes, mechanical properties, sol-gel

Xinghua Wu[1], Yuxin Tang[1], Vadim V. Silberschmidt[2], Peter Wilson[3], Zhong Chen[1]*

Mechanically Robust Transparent Anti-icing Coatings: Roles of Dispersion status of Titanate Nanotubes